



Full Length Article

Flame emission spectroscopy analysis of distributed liquid fuel combustion

Gyöngyvér Tóthpálné Hidegh^{a,*}, Bertalan Pizág^b, Ágnes Urbin^b, Erika Rácz^a, Viktor Józsa^a^a Department of Energy Engineering, Faculty of Mechanical Engineering, Budapest University of Technology and Economics, Műegyetem rkp. 3., H-1111 Budapest, Hungary^b Department of Mechatronics, Optics, and Mechanical Engineering Informatics, Faculty of Mechanical Engineering, Budapest University of Technology and Economics, Műegyetem rkp. 3., H-1111 Budapest, Hungary

ARTICLE INFO

Keywords:

Turbulent combustion
Excited species
Flame chemiluminescence

ABSTRACT

Distributed combustion offers ultra-low pollutant emission, low susceptibility of thermoacoustic instabilities, and is highly fuel flexible, being an ideal choice for, e.g., boilers, furnaces, and gas turbines. It was recently demonstrated that Mixture Temperature-Control could also achieve distributed combustion and not restricted to Moderate or Intense, Low-oxygen Dilution combustion. The former approach is employed in the present paper. Online flame control is required by the need for dynamic operation, which is often performed via spectral flame measurements. Presently, the distribution of OH*, CH*, C₂*, O₂*, and two H₂O* chemiluminescent emission peaks were evaluated; the first two represent ignition, while the latter four appear later in the reaction zone. Characteristics of distributed flames are compared to those of straight and V-shaped flames, which are well-known in the literature. The following observations were made. Distributed combustion is lifted and occupies the entire cross-section of the combustion chamber without featuring a characteristic shape. The OH*/CH* ratio shows a low dependence on the equivalence ratio, and the reactions start only 50 mm downstream of the burner lip. The dominant radical was CH* for all distributed flames. As the equivalence ratio increases, the reaction zone moves slightly upstream.

1. Introduction

84% of our total energy use is related to combustion, including 6.3% traditional biomass and 0.65% advanced biofuel utilization [1]. Therefore, meeting climate neutrality is expected no earlier than the second half of the 21st century [2,3]. A dramatic upscaling in biofuel production is expected in the upcoming decades, principally to supply transportation with renewable fuels [4]. Chemically and physically similar renewable fuels are usually compatible with existing engines, and characterized by similar emissions [5]. Since combustion will power numerous applications in the upcoming decades, developing novel combustion concepts and upgrading existing systems for cleaner and more efficient operation is a highly important task [6,7].

Safe and reliable operation requires an online combustion monitoring system [8]. The most critical parameter to control is the equivalence ratio, ϕ , since it is the key to stable operation with low emission [9]. Optical tools should be used for this purpose if real-time data is required, which is often desired in practice [10]. Among these, flame emission spectrometry, FES, is the most versatile and robust method [11]. It works as follows. Excited radicals, R^* , are formed during

combustion, which emits a photon when they reach the ground state:



where R is the radical, h is the Planck constant, and ν is the wavelength of the emitted photon. Depending on the radical and the atomic structure, the chemiluminescent emission may feature continuous or broadband emission in both the visible, ultraviolet, and infrared electromagnetic spectrum [10]. The life of the excited radicals is in the range of 10^{-8} to 10^{-6} s, meaning that chemiluminescent emission characterizes the local conditions [12]. Therefore, the biasing convective effects are negligible.

The heat release correlates well with OH* and CH* [13], and their ratio is widely used to determine ϕ ; therefore, the effect of thermal power can be canceled [14,15]. Generally, OH*/CH* properly correlates with ϕ in the case of gaseous fuel combustion [16,17], while liquid fuels behave differently due to droplet combustion and the less homogeneous fuel-air mixture [18]. Consequently, checking the OH*/CH* of distributed combustion is critical since such flames feature much more homogeneous mixtures for liquid fuels. The distribution of OH* [19], CH*

* Corresponding author.

E-mail address: hidegh.gyongyvver@gpk.bme.hu (G. Tóthpálné Hidegh).<https://doi.org/10.1016/j.fuel.2023.129193>

Received 25 April 2023; Received in revised form 17 June 2023; Accepted 7 July 2023

Available online 11 July 2023

0016-2361/© 2023 The Authors. Published by Elsevier Ltd. This is an open access article under the CC BY license (<http://creativecommons.org/licenses/by/4.0/>).

[20], and C_2^* [21] are frequently used to characterize the spatial flame structure. These radicals are formed during the following reactions [22,23]:



Reaction 8 is the conservation of the angular momentum of the electron [24]; the CO_2^* usually shows a broadband emission in the 350–600 nm wavelength range [10], which was visible in all our spectra.

The Arrhenius parameters of R1–R5 are available in [22]. Unfortunately, information on the formation of other investigated radicals in this paper is absent in the literature. The chemiluminescent emission of various radicals in hydrocarbon flames is summarized by Gaydon [24], which provided the basis for identifying the source of different characteristic spectral peaks in the present study. The radicals are present in various intensities across the flame and are sensitive to fuel composition [25]. To overcome the difficulties of various configurations, regression analysis can be used for the entire recorded spectrum [26]. Deep learning is also an option, which was successfully employed by Yoon et al. [11] for calibration processes to enable more accurate pressure and ϕ measurements. Liu et al. [27] conducted numerical simulations on laminar methane/air flames by applying deep learning. They found that the heat release rate can be characterized by OH^* and CH^* chemiluminescence. However, turbulent flames are still challenging researchers in deep learning and numerical simulations. Controlling a flame with a characteristic shape and fixed location during the operation can be performed with a fixed spectrometer. However, controlling distributed flames, which offer ultra-low emission, is more challenging since the chemiluminescent intensity is lower, the flame location is less determined, and the local intensity peaks may change their position [28]. Nevertheless, a correlation exists between local OH^* and CH^* intensities and NO_x emission [29].

It was recently demonstrated that distributed combustion could be achieved without oxygen dilution using the Mixture Temperature-Controlled, MTC, combustion concept [30]. Therefore, distributed combustion should no longer be associated with only Moderate or Intense, Low-oxygen Dilution, MILD, combustion. The advantages of the MTC combustion system compared to most MILD systems are the following. It does not require any fuel preheating, which may significantly affect the unit cost, and the fuel and air are fully premixed before the reaction zone, implying homogeneous combustion [31]. Since distributed combustion comes with lower volumetric heat release [32], the chemiluminescence intensity of the flame will be inherently low. To achieve faster response, the following two options are available. Increasing the field of view or using a more sensitive photosensor – or the combination of the two. The drawback of the former is the large integration volume, which is acceptable since distributed combustion has no characteristic shape and occupies the entire combustion chamber [30]. The obvious drawback of the more sensitive sensor is the loss of robustness and the accompanying higher unit price.

The principal goal and the novelty of this paper are to investigate the characteristics of liquid fuel distributed combustion using the MTC

combustion concept by FES. This technique is generally confined to OH^* and CH^* , while C_2^* is regularly considered in liquid fuel flames. However, the infrared part of the spectrum is barely evaluated. Therefore, three additional characteristic peaks were also investigated, two for H_2O^* and one for O_2^* . Since straight and V-shaped flames are both accessible in the MTC burner besides distributed combustion, these flames are presented for reference to highlight the spectral differences. The findings of this paper facilitate the spreading of distributed combustion in practical applications.

2. Materials and methods

The experimental combustion test rig is shown in Fig. 1. A side channel blower delivered the combustion air to provide stable inflow with low sensitivity to pressure fluctuations inside the system. Air pre-heating was performed next, using a PID-controlled preheater, which provided the 200 °C combustion air temperature (T_{ca}). The thermal power of combustion was uniform at 13.3 kW in all cases, utilizing standard diesel fuel, EN 590:2017 (D) and utility natural gas (NG) as fuels as the burner is capable of dual-fuel combustion. However, the experiments were performed in 2021, and the latest standard on diesel fuel requirements and test methods (EN 590:2022) does not contain updates relevant to the burner experiments performed. The liquid fuel flow rate was measured with an Omega FPD3202 flow meter with 2.7% uncertainty, while the FLR1204-D gas flow meter featured 2% uncertainty at a 95% level of significance after calibration. The uncertainty of the atomizing air measurement was 1 L/min, which is 1% of the full-scale value, based on the factory calibration of the Omega FMA1842A

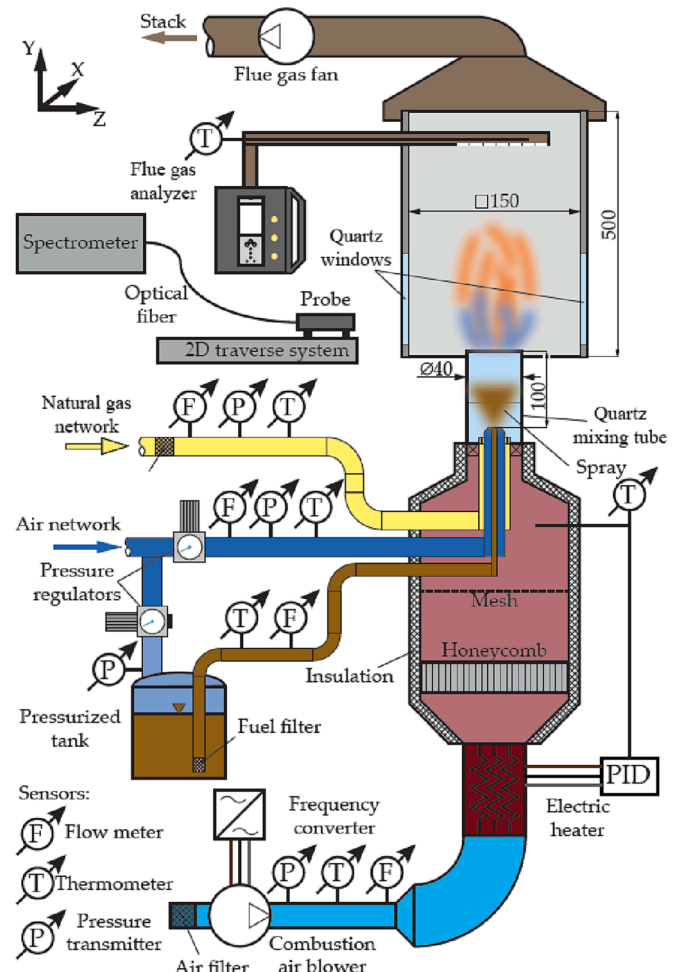


Fig. 1. Schematic diagram of the test rig based on [33].

mass flow meter. The uncertainty of atomizing air pressure measurement was less than 1 kPa, while temperature measurement was performed with less than 2 °C uncertainty for all thermometers (standard K-type thermocouples for combustion air temperature measurement and B-class Pt100 resistance thermometers for other purposes) after calibration. The combustion air was preheated in each case for D combustion, while for NG, combustion air at ambient temperature was also used.

During the tests, three different flame shapes were observed. Straight, V-shaped, and distributed. The former two are well-known in the combustion literature, using the mentioned fuels, which enables the comparison of the results with reference data. In the present study, the two air inlet streams were varied beside the fuel type. The combustion air flow rate was set based on the flue gas volumetric oxygen concentration, measured with 0.2 V/V% accuracy. Six values were set between 3 and 9 V/V%; the corresponding ϕ range is 0.57–0.86. The flame shape was varied based on ϕ and atomizing gauge pressure, p_g . The current burner configuration allowed straight and V-shaped flames for both D and NG, while distributed combustion was available only with D [33]. The settings of the cases are detailed in Table 1.

Distributed flames are lifted from the burner lip and occupy a large volume in the combustion chamber. Straight flames are connected to the burner lip with a flame root inside the mixing tube. The attached flame is also characteristic of V-shaped flames. Subsection 3.1 details the flame shapes using the images of a Nikon D7500 commercial camera with a fixed 35 mm, f/1.8 lens. The burner features a 45° axial swirler, which provides a geometric swirl number of 0.787, according to [34]. Therefore, the observed NG flames were V-shaped until the axial momentum was significantly increased by turning on the liquid fuel atomizer. The purpose of this condition was also to make the flame of the two fuels comparable to literature data.

For the optical evaluation of the flames, an Avantes AvaSpec-ULS2048CL-RS-EVO type spectrometer was used. The integration time was set to 1 s to obtain sufficient intensity levels from distributed flames of low luminosity as well. Uncertainty measurements resulted in $\pm 5\%$ arbitrary unit of chemiluminescent intensity if sufficient light gets into the sensor. The data was spectrally stable during the measurements. The combustion chamber was scanned by an optical probe following a 7×7 matrix, as shown in Fig. 2, investigating the 187–1100 nm wavelength range. The probe was calibrated with a QTH lamp in the 278–1100 nm spectral range. This encompasses UV, the entire visible, and near-infrared light. The probe was mounted on a 2D traverse system, programmed to step 15 mm in the X direction and 25 mm in the Y direction after a preliminary measurement with smaller and larger step sizes in both directions. The gradients were higher in the horizontal direction. The origin was the bottom of the window at the burner centerline. The + signs show the measurement points. The Ref point, marked with *, was used to measure the background noise, subtracted from the measured intensities. The transmittance of the heat-resistant quartz windows of the combustion chamber exceeded 90% in the 273–1100 nm wavelength range. The optical probe features a 6 mm diameter

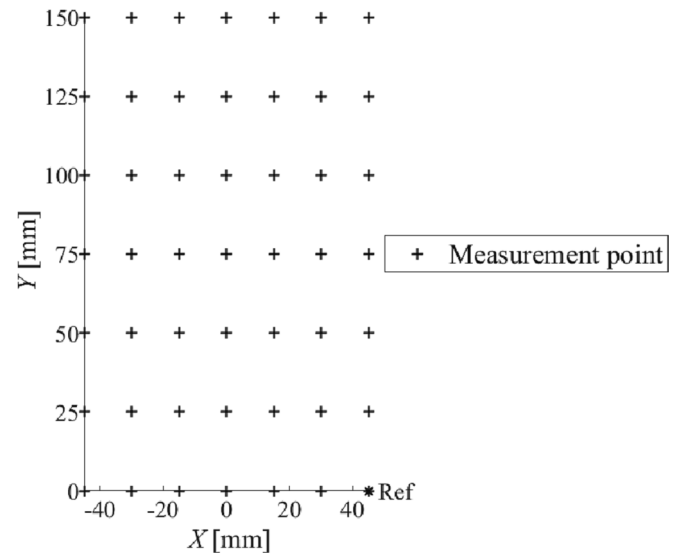


Fig. 2. The grid used for chemiluminescence measurement. ‘+’ symbols are the individual measurement points, and * refers to the Reference point, which was used to remove the background noise from the spectra.

collimating lens with a confocal length of 8.7 mm, meaning that light beams parallel to the optical axis enter the fiberglass.

The visible and invisible spectral peaks of combustion originate from various excited radicals, which originate from various characteristic chemical reactions [19] and are generated by high-temperature processes. The five highlighted radicals discussed in this paper and their respective wavelengths (three for H₂O) are listed in Table 2.

Note that the small, portable spectrometer used in this experiment had 0.58 nm spectral resolution and was not tempered, which resulted in slight sensor temperature changes. Combined with the spectral resolution, this effect leads to a few nm shifts of the intensity peaks. Therefore, a 3 nm range was scanned to find the intensity peak of each radical centered around the listed wavelengths according to the literature data in Table 2. The H₂O emission wavelength peak was altered between the two medium emission peaks at 588.02 and 590.02 nm, even in a single measurement setup at various positions in the combustion chamber. Since the above-detailed resolution and temperature biases burdened this measurement campaign, the maximum of the two was considered since the authors were unable to precisely separate the two emission peaks with the used instrument. A further possible biasing factor at 589 nm wavelength is the potential presence of sodium in the used diesel fuel. Since the esterification process for producing biodiesel uses sodium or potassium as a catalyst, the combined presence of these elements is limited to five ppm in the final fuel [35]. Nevertheless, the very strong emission of sodium might cause some bias even in marginal concentration. Since this peak was also found in natural gas combustion with similar intensity values, the effect of sodium is considered marginal.

3. Results and discussion

In this section, firstly, flame images are presented, captured by the

Table 1

Test cases and their characteristic operational parameters.

Case No.	Flue gas O ₂ [V/V %]	ϕ [1]	p_g [bar]	T_{ca} [°C]	Flame shape	Fuel
1	3	0.86	0.3	200	straight	D
2	3	0.86	0.3	23	straight	NG
3	3	0.86	0	23	V-shaped	NG
4	5	0.76	0.3	200	straight	NG
5	5	0.76	0	200	V-shaped	NG
6	5	0.76	0.6	200	distributed	D
7	6	0.71	0.6	200	distributed	D
8	7	0.67	0.6	200	distributed	D
9	8	0.62	0.6	200	distributed	D
10	9	0.57	0.6	200	distributed	D

Table 2

The investigated emission peaks of the radicals based on [24].

Radical	Wavelength according to the literature [nm]	Mean wavelength of intensity peaks [nm]
OH	309.33	310.66
CH	430.55	430.35
C ₂	516.39	515.62
H ₂ O	588.02, 590.02, 927.98	589.23, 927.97
O ₂	768.38	766.53

digital camera using identical settings. The second subsection highlights the spectra of the observed three flame shapes along the axis to reveal the reaction zone structure of each flame. Then, the spectra of all flames are compared at selected points. In Subsection 3.4, the spatial distribution of the investigated radicals, listed in Table 2, is presented along the vertical axis. Thirdly, the axial and spatial distribution of the selected radicals is shown to localize the characteristic processes in the flame. Finally, radical ratios are evaluated for all flames to characterize the local mixture quality across the combustion chamber.

3.1. Flame characteristics

Fig. 3 shows sample images of the investigated flames. The current burner could not perform distributed gaseous fuel combustion, while V-shaped D flame was omitted since preliminary analyses showed similar behavior to NG, and the present study primarily focuses on distributed combustion. The camera ISO sensitivity was set to 6400 to allow using a short, 1/1000 s exposure time, delivering more detailed spatial flame characteristics. The luminosity of the various flames in decreasing order is the following. The diesel fuel flame features burning droplets, making the flame very bright yellow. Such flames produce sufficiently high luminous intensity to use shorter integration time by spectrometers. Nevertheless, these flames are accompanied by the highest pollutant emissions, making this option less favorable for current combustion systems [33]. The reason for the high emissions is the uneven, locally rich, and hence locally high-temperature mixture that fosters both thermal and prompt NO formation. If the residence time is insufficient in the high-temperature zone of the combustion chamber, excessive CO and particulate matter emission may also be observed. The next ones are the NG flames, which show similar luminosity for both straight and V-shaped flames. It is due to the presence of the mixing tube that facilitates the mixing of the fuel and air and has sufficient length to provide a sufficiently homogeneous mixture. Therefore, as the mixture is homogeneous, flame luminosity shows a low dependence on the flame shape. Distributed flames are less luminous since the volumetric heat release rate is the lowest here. According to [31], the distributed combustion of liquid fuels will never be truly flameless due to the residual local

unevenness of the equivalence ratio since the fuel concentration is higher around the local fluid packets, which contain evaporated droplets. Consequently, fuel vapor and air mix significantly slower than in the case of a premixed gaseous fuel flame.

The blue color of the flames is caused by CH^* at 430.55 nm wavelength; it is the most dominant emitter in the visible spectrum. Yellow flames indicate local pyrolysis and soot formation due to the local absence of oxygen; the yellow color is the glowing carbon black particles. Therefore, the CH^* concentration is low here since O , O_2 , or OH is necessary to its formation, according to (R3)–(R5), respectively. CH^* can be found in the spectrum since the mixture at the flame edge is lean, but this emission peak is low, and the spectrum is dominated by the black body radiation of the soot particles, detailed in Subsection 3.2.

3.2. Chemiluminescent spectra of the flames

Fig. 4 shows the chemiluminescent spectra at several downstream distances at $X = 0$ mm of a straight, V-shaped, and distributed flame of Cases 1, 5, and 6, respectively. In the case of the straight diesel flame in Fig. 4a, broadband soot radiation dominates the spectrum, which makes the flame yellow, as was shown previously in Fig. 3. The flame root is located inside the mixing tube, indicated by the typical flame spectrum at $Y = 0$ mm. This point did not show the highest chemiluminescent intensities due to the higher flow velocities and the vicinity of the walls, which absorb the excess energy of the radicals, ultimately slowing down the reactions. Therefore, straight flames showed the highest overall intensities at $Y = 25$ and 50 mm among the investigated points. Then, as combustion progresses, the overall intensities gradually decrease downstream. Soot radiation is superposed with the emission of the characteristic radicals linearly [12]. Hence, the intensity peaks of the investigated radicals are not as outstanding in the chemiluminescent spectra as in Fig. 4b or 4c, while the chemiluminescent intensity in Fig. 4a is more intense. Moreover, different reaction pathways are present here due to the locally high equivalence ratio.

Similar to the straight D flame, the V-shaped NG flame, shown in Fig. 4b, shows the highest intensities at $Y = 25$ mm, closely followed by the spectrum at $Y = 50$ mm below 600 nm. This range features fast radicals, such as OH^* and CH^* , which have a short lifetime and quickly appear at the beginning of the reaction zone of premixed flames. Since all NG flames were properly premixed, their flame color was blue with no yellow flares, which are the indicators of local soot formation. Therefore, peaks of various radicals dominated the spectra, like in the case of distributed combustion in Fig. 4c. However, V-shaped flames are compact, meaning an increased volumetric heat release rate compared to distributed flames, implying significantly higher intensity values at the peaks.

The flame of distributed combustion is visible in the upper part of the combustion chamber. Therefore, the spectra at $Y = 0$ and 25 mm closely showed the background intensity in Fig. 4c. The characteristic peaks of hydrocarbon combustion appeared at $Y = 50$ mm and peaked at $Y = 100$ mm. All the spectra confirm the absence of soot particles; no black body radiation curve was observed, while chemiluminescent emission of characteristic radicals was observed in the spectrum. The corresponding intensities peaked at $Y = 100$ – 150 mm, which implies that the flame was clearly lifted from the burner, and the flame is not entirely confined to the chamber volume with optical access via the quartz windows. In the case of distributed combustion, fuel droplets have sufficient time to completely evaporate and mix with combustion air. Consequently, the flame is blue because the CH^* emission is the dominant intensity peak in the visible spectra.

Fig. 5 shows the spectra of the flames at all the test cases at selected measurement points. Straight and V-shaped flames are shown in Fig. 5a, while the spectra of distributed flames with various equivalence ratios are present in Fig. 5b. The most characteristic point of distributed flames was $X = 15$ mm, $Y = 150$ mm, while the other flame spectra were compared at $X = 0$ mm, $Y = 25$ mm. The spectrum of the D flame is

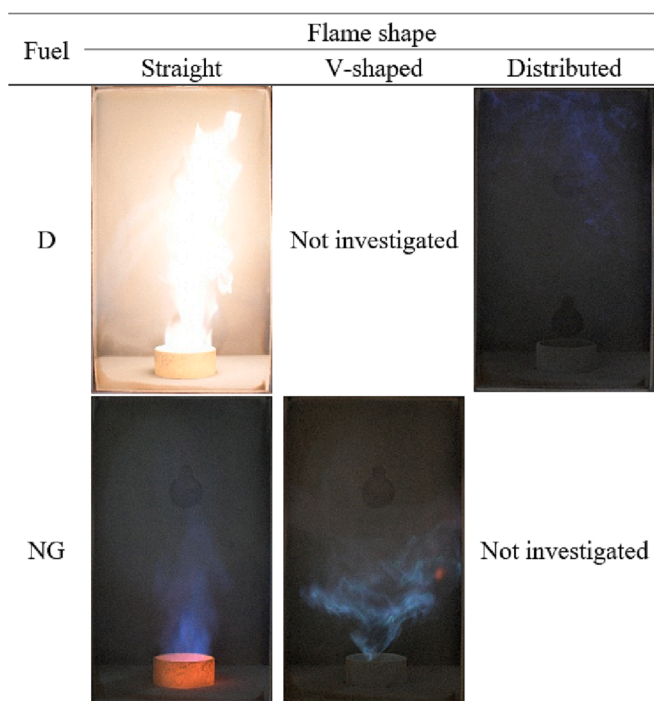


Fig. 3. Typical flame images. Each of them was captured in manual mode at $f/3.5$, ISO 6400 sensitivity, and 1/1000 s shutter speed.

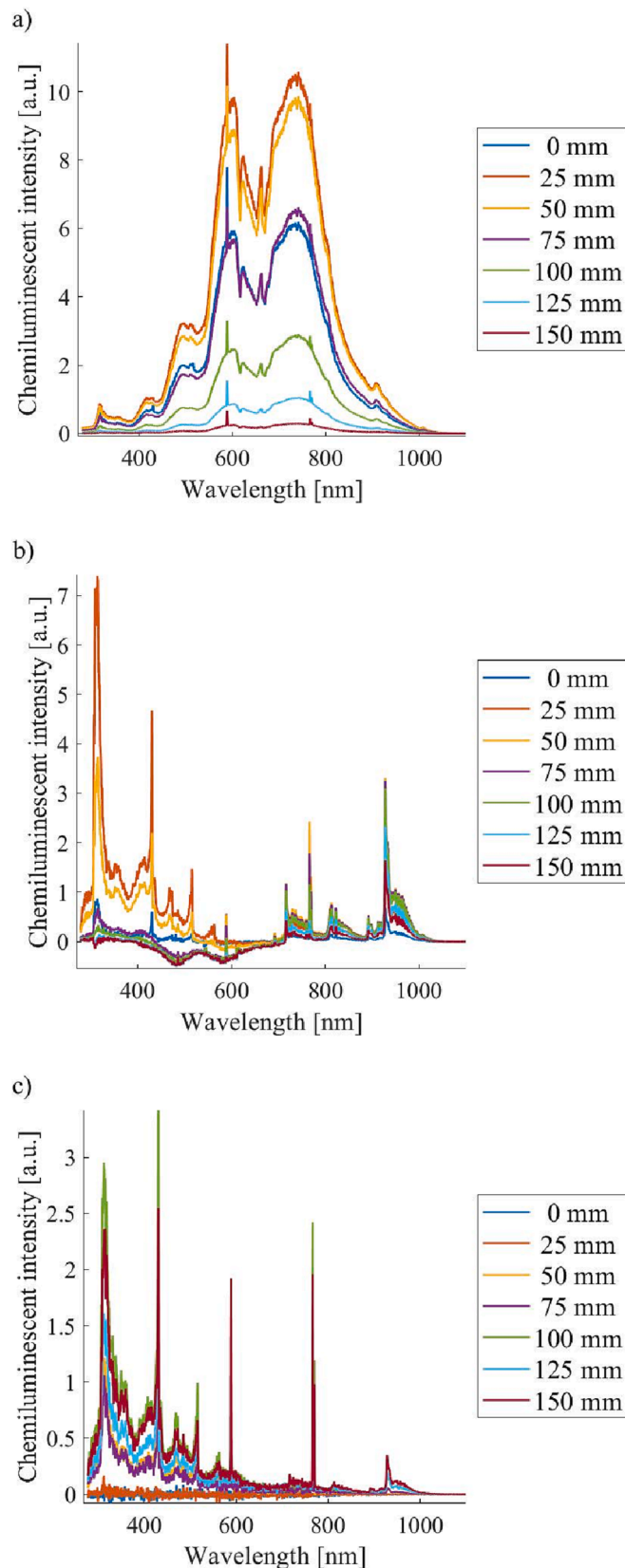


Fig. 4. Chemiluminescent spectra at $X = 0$ mm and various downstream distances in a) Case 1: straight D, b) Case 5: V-shaped NG, and c) Case 6: distributed D flames. Note that curves of $Y = 50$ and 75 mm are highly overlapping in Fig. 4c.

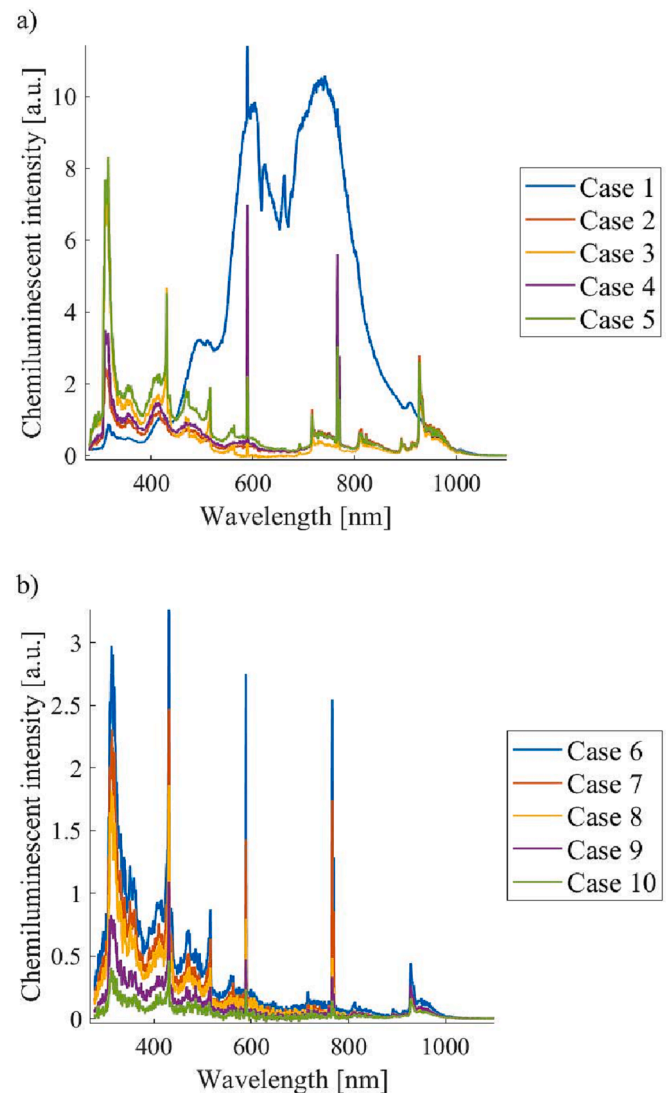


Fig. 5. Chemiluminescent spectra of the flames in a) Case 1–5 at $X = 0$ mm, $Y = 25$ mm, and b) Case 6–10 at $X = 15$ mm, $Y = 150$ mm.

different from the others due to soot formation. The CH^* peak is negligible in the spectra of flames of Case 1, 2, and 4, which are the three straight flames. Over 600 nm, the V-shaped NG flame of Case 3 without combustion air preheating shows the lowest intensity as chemiluminescent intensity depends on the reacting gas temperature [24].

The spectra of distributed combustion are highly similar to each other; the intensity values decrease as the flame becomes leaner. This result also means the leaner flame is less visible, approaching completely flameless combustion. When distributed combustion is compared to swirl flames in methane combustion, the OH^* and CH^* emission peaks significantly decrease compared to the decrease of other peaks, see Subsection 3.3 of [36]. This trend is absent in the present case. A possible explanation is the less even fuel–air mixture of liquid fuel distributed combustion since the atomized liquid fuel needs to be evaporated before mixing with the combustion air [31]. However, gaseous fuels may immediately mix with the combustion air when injected, allowing more time to form a homogeneous fuel–air mixture in the same burner compared to liquid fuel operation.

3.3. Spectral flame characteristics along the axis

Fig. 6 shows the chemiluminescent intensities of the species of Table 2 at the axis of the burner at each vertical position. Note that the

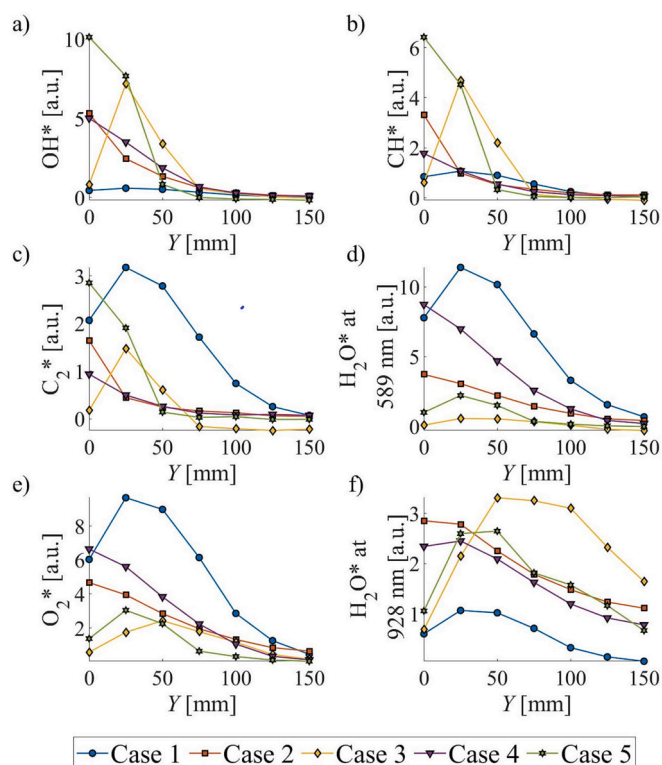


Fig. 6. Chemiluminescent intensities at the selected wavelengths of the straight and V-shaped flames in Cases 1–5 at $X = 0$ mm. Note the different vertical scales.

soot radiation of the straight D flame, Case 1, makes this flame the most luminous from $Y = 25$ mm in Fig. 6c–e, where the black body radiation effect is strong. All the radicals show a decreasing trend towards the end of the investigated zone, indicating that the intense reaction zone is well captured. Both OH^* and CH^* intensities are concentrated up to $Y = 100$ mm, meaning that the heat release is practically complete up to this point; the final reactions of the chemical conversion dominate the rest of the range.

The effect of combustion air preheating on the OH^* , CH^* , and C_2^* of straight NG flames, which are Cases 2 and 4, is marginal; the difference is the most apparent for H_2O^* emission. The V-shaped NG flames, which are Cases 3 and 5, uniformly show higher intensity values at $Y = 0$ mm for the first three radicals for Case 5, which has 200°C combustion air preheating, while the increased intensity is present only up to $Y = 50$ mm for the last three radicals. Then the intensities of the highlighted radicals of Case 3 with no combustion air preheating surpass those of Case 5 as air preheating speeds up all reactions, and the heat release is more concentrated around the burner lip.

The chemiluminescent intensity of all species of Table 2 is presented along the axis at all downstream distances for each distributed combustion case in Fig. 7. All data sets show that marginal intensity up to $Y = 25$ mm compared to the background noise. The different vertical axis values show that CH^* has the highest intensity in the visible spectrum and is the dominant radical overall. The mixture ignition occurs earlier in Cases 6–8 since the mixture is richer than in Cases 9 and 10. The results clearly indicate that the flame of Cases 9 and 10 is elongated, and the reactions occur slowly. Since all trends show an increase up to $Y = 150$ mm, the most intense part of the reaction zone is present in the downstream part of the combustion chamber. As for Cases 6–8, the chemiluminescent intensities increase with ϕ , and the peak values of OH^* , CH^* , and C_2^* are located within the investigated region. The two H_2O^* peaks, shown in Fig. 7d and 7f, indicate that complete combustion did not occur by $Y = 150$ mm. The only outlier is Case 7, which will be

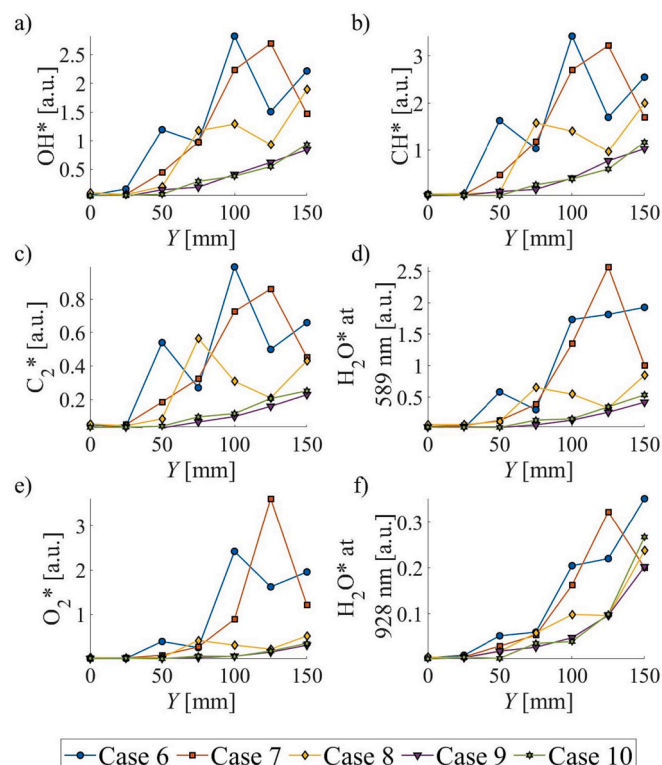


Fig. 7. Chemiluminescent intensities at selected wavelengths of all distributed combustion cases at $X = 0$ mm. Note the different vertical scales.

further analyzed in Subsection 3.4.

3.4. Spatial distribution of the highlighted radicals

Subsections 3.4 and 3.5 feature contour plots of various cases, which are colored differently. The contour lines of various intensity levels compared to the highest values are added, allowing the overview of the distributions of various highlighted radicals, which is crucial for the proper chemiluminescence sensor position. The filling is used only within the 80% and 90% contour lines; below 80%, only the contour line type was varied to allow easier reading of the figures since many regions overlap below this threshold. Note that measurements were only performed at points marked with a + symbol, and the plot was generated by the *contourf* Matlab function using quadratic curves [37].

Fig. 8 shows the spatial distribution of the six highlighted radicals of the straight and V-shaped flames. The straight D flame, Case 1, showed a clear, straight radical distribution. The position of the zones was moved downstream with the increase in wavelength, indicating that OH^* formation is the fastest process, while H_2O^* formation is the slowest, as this radical is the product of a chain termination reaction. The intense zones downstream of the burner lip show that the highest heat release occurs later as the droplets need time for evaporation, then the fuel vapor needs to be mixed with combustion air. Since NG only needs to be mixed with air, straight NG flames, which are Cases 2 and 4, feature the peak intensities at $Y = 0$ mm, implying that the most intense reaction zone is within the mixing tube. The regions with the highest intensity of the V-shaped flames are located at the burner lip for the first three radicals with combustion air preheating. Without it, these characteristic features are present downstream along the stems of the V, and the high-intensity zones are larger as the reactions occur slower. The low intensity contour lines always follow the flame shape in the case of both straight and V-shaped flames.

Fig. 9 follows the trends presented in Fig. 7, i.e., the reaction zone is absent up to $Y = 25$ mm. Cases 6–8 are also separated here from Cases 9

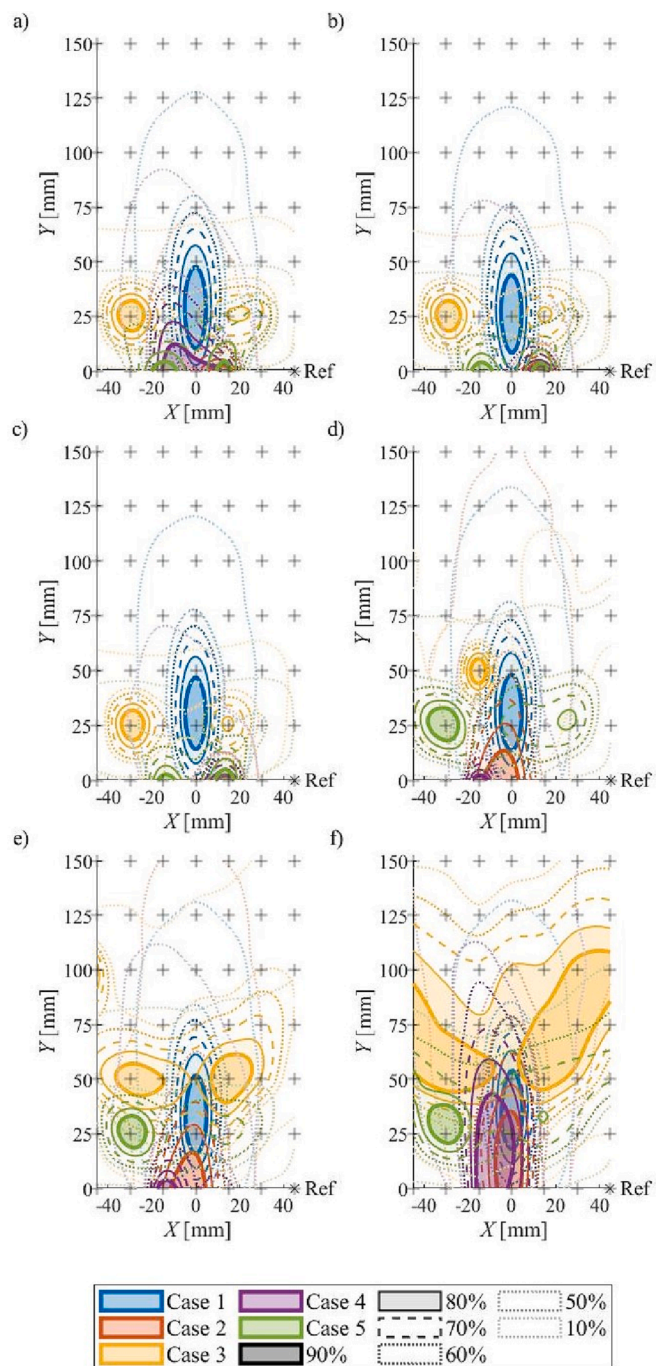


Fig. 8. Distribution of radicals in the combustion chamber in Cases 1–5. a) OH^* , b) CH^* , c) C_2^* , d) H_2O^* at 589.26 nm, e) O_2^* , and f) H_2O^* at 927.98 nm.

and 10, as the peaks and the interpolated zones are mostly located at $Y = 150$ mm. As the flame becomes leaner, the centers of the radical emissions shift downstream in the combustion chamber due to the increased air flow rate and the lower reactivity of the mixture. Case 7 shows an intensity peak at $Y = 125$ mm for each radical, which makes this case an outlier, as the emission peaks move downstream with increasing wavelengths in the other cases. However, Cases 6 and 8 are an exception to the C_2^* and O_2^* emission distribution, respectively, as presented in Fig. 7c and e.

Distributed combustion is not well-localized; therefore, the low-intensity contour lines are not following the shape of the high-intensity regions, unlike in the other flame shapes, shown in Fig. 8. The peaks are not uniformly present at the axis; these can be found in

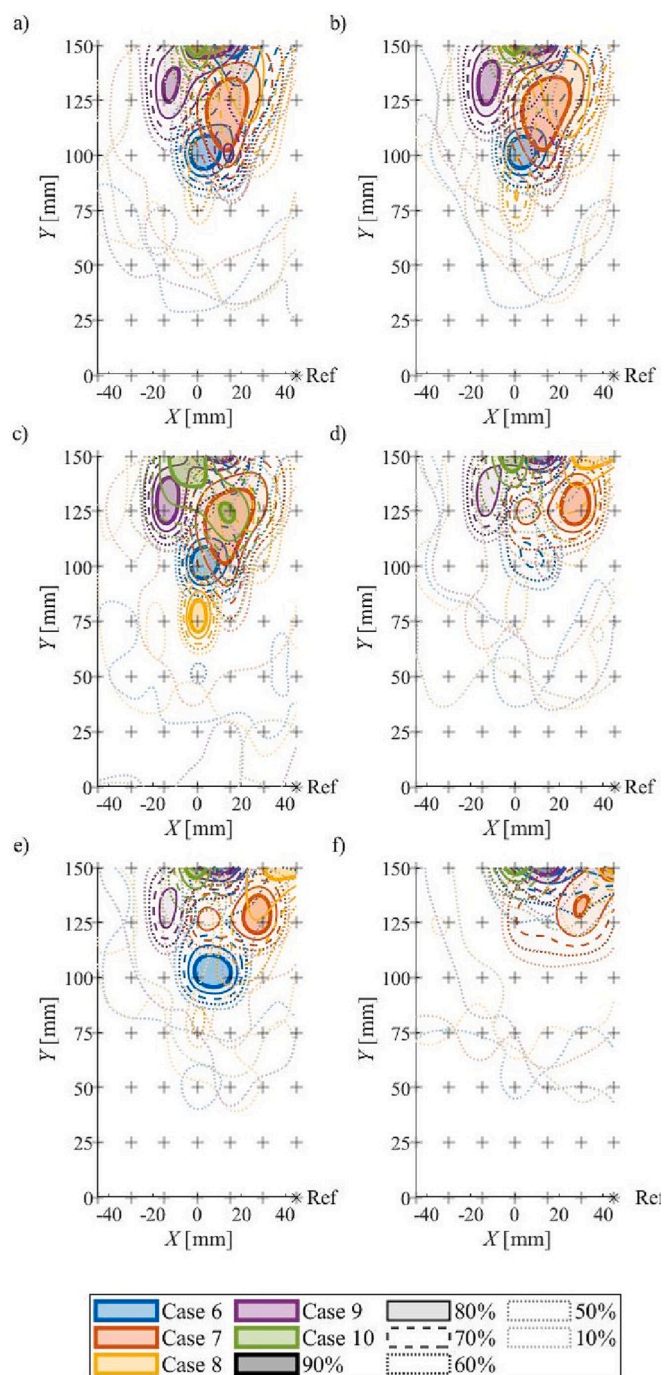


Fig. 9. Distribution of radicals in the combustion chamber in Cases 6–10. a) OH^* , b) CH^* , c) C_2^* , d) H_2O^* at 589.26 nm, e) O_2^* , and f) H_2O^* at 927.98 nm.

both sides. If lower intensity values are checked, the contour lines encompass wide areas instead of vertical shapes, which are typical for classical flames.

3.5. OH^*/CH^* intensity ratio distribution

Fig. 10 shows the OH^*/CH^* intensity ratio along the axis, which is a widely used radical ratio to determine the local equivalence ratio of gaseous flames, mentioned in the Introduction. Note that the intensity ratio was set to zero if the intensity of either of the radicals is lower than 1% of the maximum intensity value to avoid excessive OH^*/CH^* fluctuations due to the small values of both radicals. In Fig. 10a, the straight

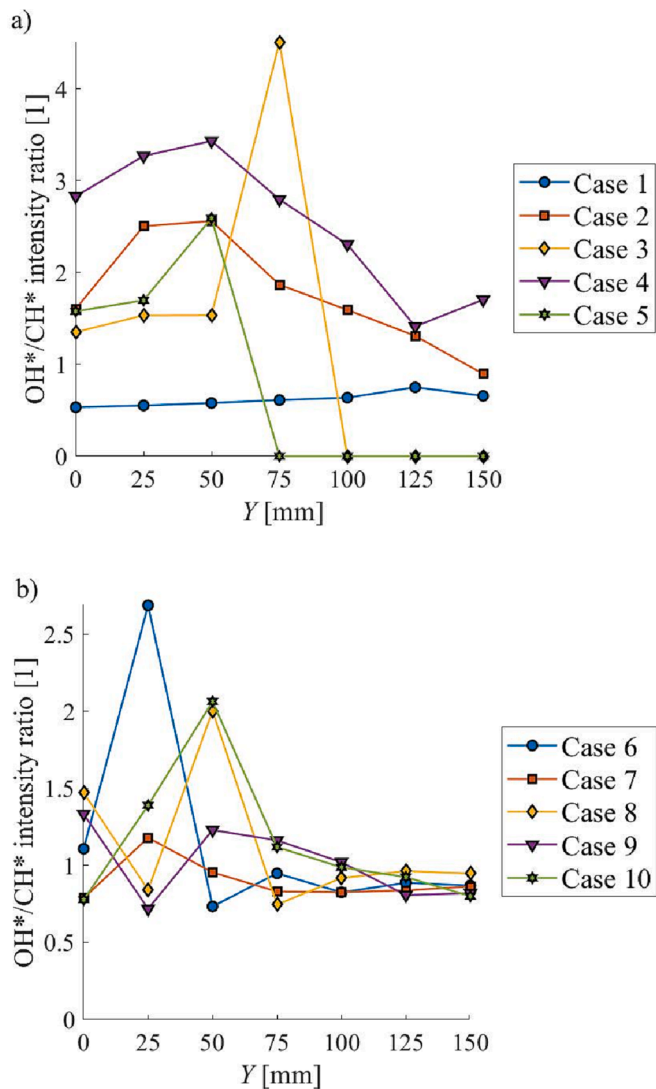


Fig. 10. OH*/CH* intensity ratios at $X = 0$ mm in a) Cases 1–5, b) Cases 6–10.

D flame, Case 1, features a nearly flat trend around 0.8, meaning low OH* concentration due to the locally rich reaction zone with soot formation. Zhang et al. [38] investigated the OH*, CH*, and C₂* emission of CH₄/O₂ co-flow diffusion flames, and they concluded that in line with premixed flame characteristics, the local O/C ratio at the flame axis could be characterized quantitatively by the OH*/CH* ratio. However, no apparent trends were found in Cases 2 and 4 of straight NG flames, even though 97 V/V% of the utility NG is CH₄. They, and the flame of Case 5, feature a peak at $Y = 25$ – 75 mm, and the ratio starts decreasing, making the sensor position dependent on location in the flame.

The distributed flames are characterized by different trends, as shown in Fig. 10b, Cases 6–10 feature gradually decreasing ϕ ; therefore, higher OH*/CH* values are expected with higher case numbers. However, the presented trends differ; the values scatter between 0.6 and 1.3 from $Y = 75$ mm. Consequently, the expected trend is absent in the case of distributed flames, meaning that these flames cannot be controlled based on the OH*/CH* ratio. Even though the OH*/CH* ratio is often used as a quality indicator, the quantitative trends showed no apparent trend. The relatively flat trend indicates a homogeneous reaction zone. Tu et al. [36] observed flat trends as a function of thermal power and ϕ in the case of MILD methane combustion, including other radical ratios, such as C₂*/OH* and C₂*/CH*. These and further radical ratios, including H₂O* and O₂*, showed similar trends at the axis. Since their spatial distribution also showed fluctuating trends, only the OH*/CH*

ratios are presented below. These findings imply that spectral evaluation methods working for non-distributed combustion must be revisited since the reaction zone behaves differently. All visualized radicals, radical ratios, and the corresponding data are included in the [Supplementary material](#) of this paper.

Fig. 11 shows the OH*/CH* intensity ratios of Cases 1–5. The OH*/CH* ratio distribution of straight NG flames is peaking along the visible

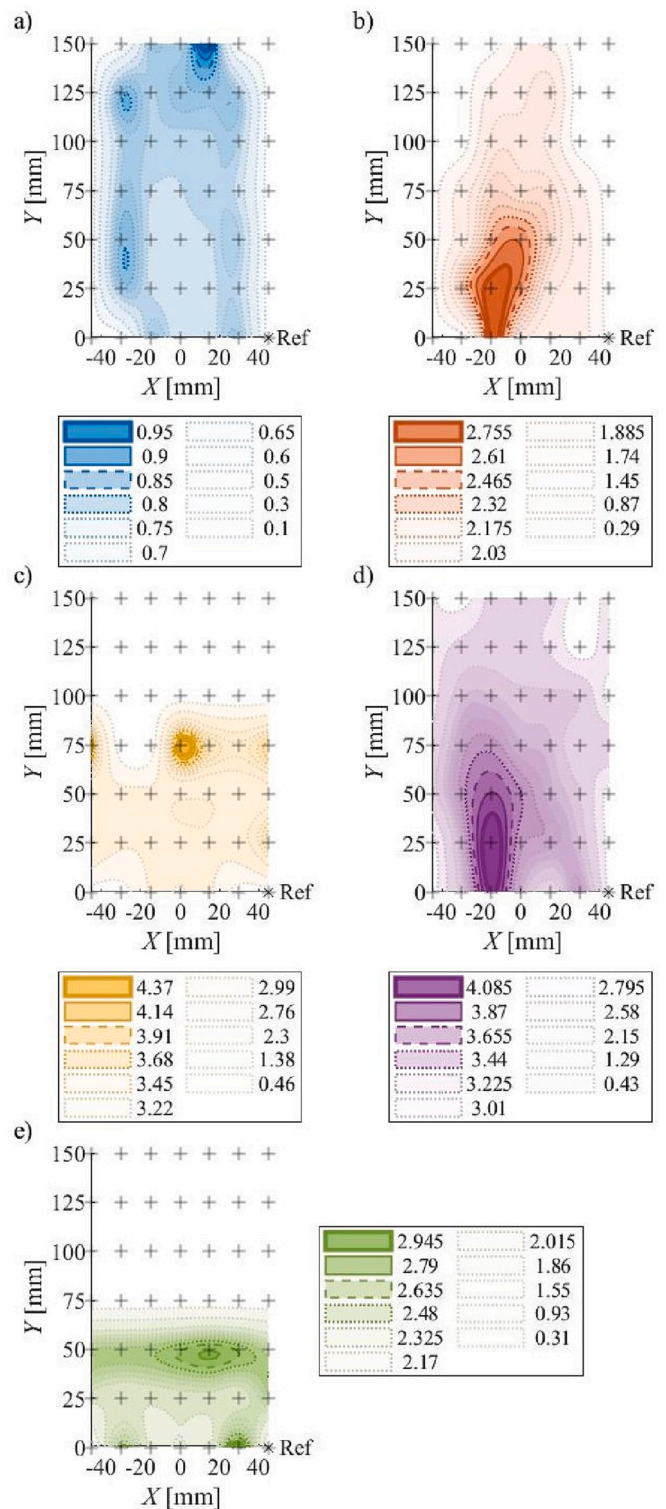


Fig. 11. OH*/CH* intensity ratios in a) Case 1, b) Case 2, c) Case 3, d) Case 4, and e) Case 5.

flame body and shows a significant variation with X due to the high horizontal gradients in straight flames. The relative presence of OH^* to CH^* is higher than the unity for all flames. Fig. 11a implies a relatively homogenous mixture across the control volume, excluding one peak at $X = 30$ mm, $Y = 125$ mm, and the lower intensity ratio area at the flame root, where the mixture was locally richer in fuel, resulting in relatively higher CH^* emission intensity to the outer flame. The OH^*/CH^* ratios of V-shaped flames are peaking at the tip of the V or in the recirculation zone at the flame side, and the high-intensity zone is horizontal. The dominance of OH^* is also present in these flames, like in the case of straight NG flames. The axial variation shown in Fig. 10a is similar to other $X = \text{constant}$ lines. Therefore, sensor placement is the least critical for V-shaped flames.

The asymmetry of the straight NG flames, Cases 2 and 4 in Fig. 11, is most probably due to hydrodynamic instability since the geometry is symmetrical. The majority of the mass flow is present near the mixing tube wall in a swirl burner due to the inertia of the flowing medium. Small imperfections break the symmetry of this annular flow of the burner assembly. Therefore, asymmetry of various flame types is typical in both in-house-built burners [39] and stock burners [40].

Fig. 12 shows the OH^*/CH^* intensity ratios of Cases 6–10. The high-intensity colored part gradually shrinks with decreasing ϕ , implying a less homogeneous mixture across the control volume. Therefore, local hot spots are emerging, which are randomly distributed. Nevertheless, the quantitative difference between these flames is small; the peak OH^*/CH^* ratio is around unity, as presented in Fig. 10b. Flame homogeneity was presented for distributed flames with no apparent change with ϕ .

It was presented that distributed combustion is cumbersome to control based solely on one radical or radical ratio. Consequently, a solution can be evaluating the entire spectrum using regression analysis [26] or an artificial intelligence-based algorithm [41]. However, such solutions are confined to the given application or burner type. A combined method can be used to overcome these difficulties, such as adding a microphone signal and evaluating the two at once [10]. Finally, online control of distributed combustion requires further research since the classical techniques cannot be directly employed here due to the low flame luminosity.

4. Conclusions

This paper presented the flame emission spectrometry analysis of nearly-flameless liquid fuel combustion using standard diesel fuel. For reference, straight and V-shaped flames were also included. Based on the results, the following conclusions were derived.

1. Distributed flames at $Y = 0$ and 25 mm showed the background intensity closely. The intensity of the investigated radicals peaked at $Y = 100$ –150 mm, proving that the flame was clearly lifted from the burner lip to downstream parts of the combustion chamber. The flame root of straight and V-shaped flames is located inside the mixing tube. The integral of the spectra was the largest at $Y = 25$ mm, right after the mixing tube.
2. The pyrolysis inside straight flames is due to the locally high equivalence ratio that leads to vanishing CH^* and C_2^* peaks in the spectra in the $Y = 25$ –75 mm range.
3. CH^* has the highest intensity in the visible spectrum of distributed flames and is the dominant radical overall. The two H_2O^* peaks indicate that complete combustion did not occur by $Y = 150$ mm, which was the top of the chamber window.
4. Complete combustion of straight and V-shaped flames occurs within the investigated zone, indicated by all radicals. OH^* and CH^* intensities are concentrated up to $Y = 75$ mm, meaning that the heat release is practically complete up to this point.
5. As a distributed flame becomes leaner, the centers of the radical emissions shift downstream in the combustion chamber due to the increased air flow rate and the lower reactivity of the mixture. If the

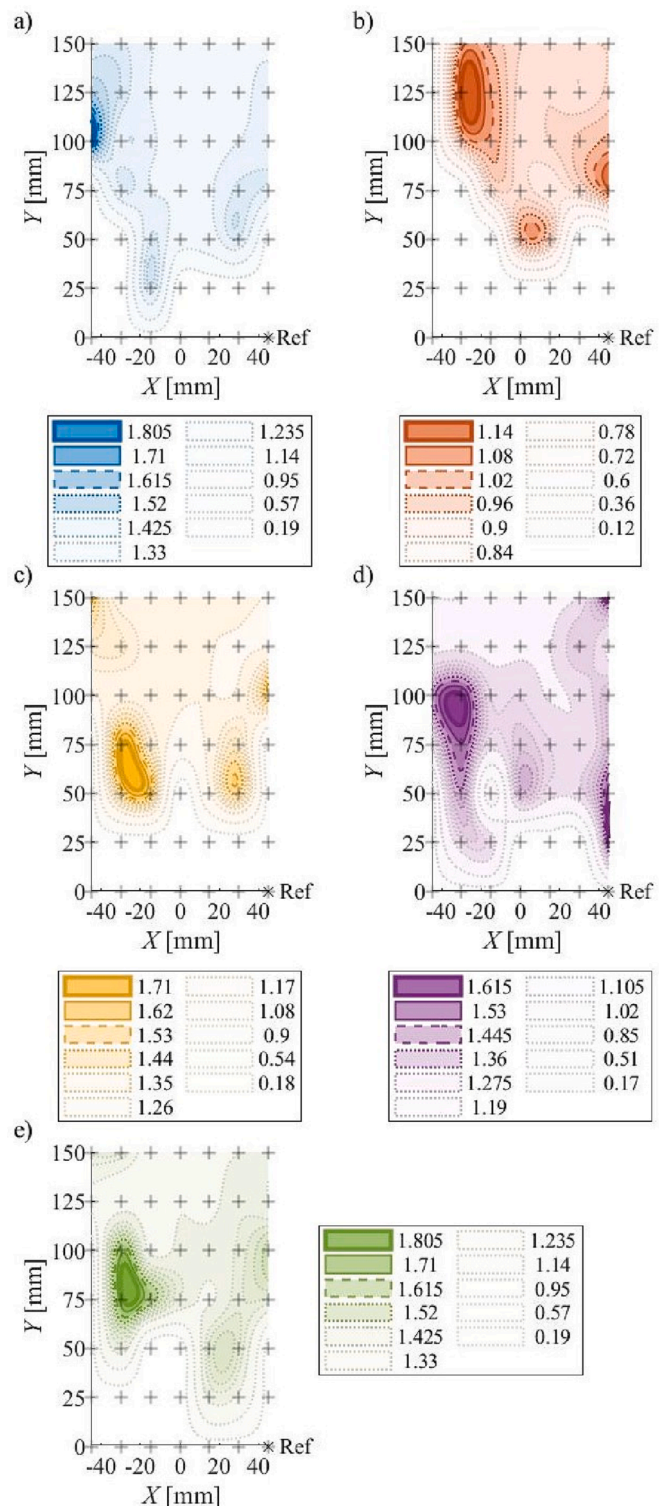


Fig. 12. OH^*/CH^* intensity ratios in a) Case 6, b) Case 7, c) Case 8, d) Case 9, and e) Case 10.

reaction zone boundaries are checked, the contour lines of distributed flames encompass wide areas instead of well-localized shapes, characteristic of straight and V-shaped flames.

6. Distributed flame cases feature similar OH^*/CH^* ratios in the reaction zone even with varying ϕ , meaning that equivalence ratio control by radical ratio is impossible for these flames.

Funding

The research reported in this paper was supported by the National Research, Development and Innovation Fund of Hungary, project N^os OTKA-FK 137758 and TKP-6-6/PALY-2021 under the TKP2021-NVA funding scheme from the National Research, Development and Innovation Fund, N^os. ÚNKP-22-5-BME-304 and ÚNKP-22-3-II-BME-113, supported by the New National Excellence Program of the Ministry for Culture and Innovation from the source of the National Research, Development and Innovation Fund, and the János Bolyai Research Scholarship of the Hungarian Academy of Sciences.

CRediT authorship contribution statement

Gyöngyvér Tóthpálné Hidegh: . **Bertalan Pizág:** Validation, Software, Resources, Formal analysis, Investigation. **Ágnes Urbin:** Validation, Resources, Investigation, Data curation. **Erika Rácz:** Validation, Resources, Investigation. **Viktor Józsa:** Writing – original draft, Writing – review & editing, Validation, Resources, Project administration, Methodology, Investigation, Funding acquisition, Conceptualization.

Declaration of Competing Interest

The authors declare that they have no known competing financial interests or personal relationships that could have appeared to influence the work reported in this paper.

Data availability

Data will be made available on request.

Appendix A. Supplementary data

Supplementary data to this article can be found online at <https://doi.org/10.1016/j.fuel.2023.129193>.

References

- [1] Ritchie H, Roser M, Rosado P. Energy production and consumption. our. World Data 2022.
- [2] Buira D, Tovilla J, Farbes J, Jones R, Haley B, Gastelum D. A whole-economy deep decarbonization pathway for Mexico. Energy Strateg Rev 2021;33:100578. <https://doi.org/10.1016/j.esr.2020.100578>.
- [3] Pan X, Wang H, Wang L, Chen W. Decarbonization of China's transportation sector: In light of national mitigation toward the Paris Agreement goals. Energy 2018;155: 853–64. <https://doi.org/10.1016/j.energy.2018.04.144>.
- [4] Pfleger BF, Takors R. Recent progress in the synthesis of advanced biofuel and bioproducts. Curr Opin Biotechnol 2023;80:102913. <https://doi.org/10.1016/j.copbio.2023.102913>.
- [5] Berghthorson JM, Thomson MJ. A review of the combustion and emissions properties of advanced transportation biofuels and their impact on existing and future engines. Renew Sustain Energy Rev 2015;42:1393–417. <https://doi.org/10.1016/j.rser.2014.10.034>.
- [6] Lefebvre AH, Ballal DR. Gas turbine combustion. third. Boca Raton: CRC Press; 2010. <https://doi.org/10.1201/9781420086058>.
- [7] Cerinski D, Vujanović M, Petranović Z, Baleta J, Samec N, Hriberšek M. Numerical analysis of fuel injection configuration on nitrogen oxides formation in a jet engine combustion chamber. Energy Convers Manag 2020;220:112862.
- [8] Xia Y, Zhang J, Tang C, Pan W. Research and application of online monitoring of coal and biomass co-combustion and biomass combustion characteristics based on combustion flame. J Energy Inst 2023;108:101191.
- [9] Lopez-Ruiz G, Alava I, Blanco JM. Impact of H₂/CH₄ blends on the flexibility of micromix burners applied to industrial combustion systems. Energy 2023;270. <https://doi.org/10.1016/j.energy.2023.126882>.
- [10] Ballester J, García-Armingol T. Diagnostic techniques for the monitoring and control of practical flames. Prog Energy Combust Sci 2010;36:375–411. <https://doi.org/10.1016/j.pecs.2009.11.005>.
- [11] Yoon T, Kim SW, Byun H, Kim Y, Carter CD, Do H. Deep learning-based denoising for fast time-resolved flame emission spectroscopy in high-pressure combustion environment. Combust Flame 2023;248:112583. <https://doi.org/10.1016/j.combustflame.2022.112583>.
- [12] Grauer SJ, Mohri K, Yu T, Liu H, Cai W. Volumetric emission tomography for combustion processes. Prog Energy Combust Sci 2023;94:101024. <https://doi.org/10.1016/j.pecs.2022.101024>.
- [13] Kumar M, Karmakar S. Butyl butyrate, Jet A-1 and their blends: Combustion performance in the swirl stabilized burner at different inlet air temperature. Biomass Bioenergy 2023;168:106651. <https://doi.org/10.1016/j.biombioe.2022.106651>.
- [14] Guyot D, Guethe F, Schuermans B, Lacarelle A, Paschereit CO. CH^{*}/OH^{*} Chemiluminescence response of an atmospheric premixed flame under varying operating conditions. Proceedings ASME Turbo EXPO 2010:1–12. <https://doi.org/10.1115/GT2010-23135>.
- [15] Parameswaran T, Gogolek P, Hughes P. Estimation of combustion air requirement and heating value of fuel gas mixtures from flame spectra. Appl Therm Eng 2016; 2015:353–61. <https://doi.org/10.1016/j.applthermaleng.2014.11.034>.
- [16] Muruganandam TM, Kim B-H, Morrell MR, Nori V, Patel M, Romig BW, et al. Optical equivalence ratio sensors for gas turbine combustors. Proc Combust Inst 2005;30(1):1601–9.
- [17] Souflas K. Experimental investigation of OH^{*}/CH^{*} ratio variations in turbulent, disk stabilized, lean propane-air flames with inlet mixture preheat and stratification. Exp Therm Fluid Sci 2022;136:110670. <https://doi.org/10.1016/j.expthermflusci.2022.110670>.
- [18] Józsa V, Kun-balog A. Spectroscopic analysis of crude rapeseed oil flame. Fuel Process Technol 2015;139:61–6. <https://doi.org/10.1016/j.fuproc.2015.08.011>.
- [19] Gao L, Yu X, Peng J, Tian Ye, Cao Z, Zhong F, et al. Flame characteristics of a cavity-based scramjet combustor using OH-PLIF and feature extraction. Int J Hydrogen Energy 2022;47(47):20662–75.
- [20] Chong CT, Hochgreb S. Spray combustion characteristics of palm biodiesel. Combust Sci Technol 2012;184:1093–107. <https://doi.org/10.1080/00102202.2012.663999>.
- [21] Reyes J, Kumar Abhinavam Kailasanathan R, Ahmed K. Relationship between the chemiluminescence intensity ratio of C₂^{*} and CH^{*}, charge pressure, and equivalence ratio for gasoline. Energy Fuel 2018;32:10933–40. <https://doi.org/10.1021/acs.energyfuels.8b00729>.
- [22] Panoutsos CS, Hardalupas Y, Taylor AMKP. Numerical evaluation of equivalence ratio measurement using OH^{*} and CH^{*} chemiluminescence in premixed and non-premixed methane-air flames. Combust Flame 2009;156:273–91. <https://doi.org/10.1016/j.combustflame.2008.11.008>.
- [23] Kathrotia T, Riedel U, Seipel A, Moshhammer K, Brockhinke A. Experimental and numerical study of chemiluminescent species in low-pressure flames. Appl Phys B Lasers Opt 2012;107:571–84. <https://doi.org/10.1007/s00340-012-5002-0>.
- [24] Broida HP. The spectroscopy of flames. Combust Flame 1975;25:283.
- [25] Breaux BB, Acharya S. The effect of elevated water content on swirl-stabilized ethanol/air flames. Fuel 2013;105:90–102. <https://doi.org/10.1016/j.fuel.2012.07.051>.
- [26] Tripathi MM, Krishnan SR, Srinivasan KK, Yueh FY, Singh JP. Chemiluminescence-based multivariate sensing of local equivalence ratios in premixed atmospheric methane-air flames. Fuel 2012;93:684–91. <https://doi.org/10.1016/j.fuel.2011.08.038>.
- [27] Liu Y, Tan J, Wang H, Lv L. Characterization of heat release rate by OH^{*} and CH^{*} chemiluminescence. Acta Astronaut 2019;154:44–51. <https://doi.org/10.1016/j.actaastro.2018.10.022>.
- [28] Feser JS, Karyeyen S, Gupta AK. Flowfield impact on distributed combustion in a swirl assisted burner. Fuel 2020;263:116643. <https://doi.org/10.1016/j.fuel.2019.116643>.
- [29] Ariemma GB, Sorrentino G, de Joannon M, Sabia P, Albano A, Ragucci R. Optical sensing for MILD Combustion monitoring. Fuel 2023;339:127479. <https://doi.org/10.1016/j.fuel.2023.127479>.
- [30] Józsa V. Mixture temperature-controlled combustion: a revolutionary concept for ultra-low NO_x emission. Fuel 2021;291:120200.
- [31] Wang F, Li P, Wang G, Mi J. Moderate and intense low-oxygen dilution (MILD) combustion of liquid fuels: a review. Energy Fuel 2022;36:8026–53. <https://doi.org/10.1021/acs.energyfuels.2c01383>.
- [32] Reddy VM, Trivedi D, Sawant D, Kumar S. Investigations on emission characteristics of liquid fuels in a swirl combustor. Combust Sci Technol 2015;187: 469–88. <https://doi.org/10.1080/00102202.2014.956098>.
- [33] Hidegh G, Csemány D, Vámos J, Kavas L, Józsa V. Mixture temperature-controlled combustion of different biodiesels and conventional fuels. Energy 2021;234: 121219.
- [34] Beér JM, Chigier NA. Combustion aerodynamics. London: Robert E. Krieger Publishing Company, Inc.; 1972.
- [35] Barker J, Cook S, Richards P. Sodium contamination of diesel fuel, its interaction with fuel additives and the resultant effects on filter plugging and injector fouling. SAE Int J Fuels Lubr 2013;6:826–38. <https://doi.org/10.4271/2013-01-2687>.
- [36] Tu Y, Liu H, Zhu Y, Guiberti TF, Roberts WL. MILD combustion of methane in a model combustor with an inverse-diffusion flame configuration. Fuel 2022;328: 125315. <https://doi.org/10.1016/j.fuel.2022.125315>.
- [37] MathWorks. MATLAB, Release 2022b 2022.
- [38] Zhang T, Guo Q, Liang Q, Dai Z, Yu G. Distribution characteristics of OH^{*}, CH^{*}, and C₂^{*} luminescence in CH₄/O₂ 2 co-flow diffusion flames. Energy Fuel 2012;26: 5503–8. <https://doi.org/10.1021/ef300970a>.
- [39] Huang M, Li R, Xu J, Cheng S, Deng H, Rong Z, et al. Effect of equivalence ratio and staging ratio on the methane MILD combustion in dual-stage combustor. Fuel 2022;307:121903. <https://doi.org/10.1016/j.fuel.2021.121903>.
- [40] Józsa V, Kun-Balog A. Effect of quarks on the blowout stability and emission of pollutants of a liquid-fueled swirl burner. J Eng Gas Turbines Power 2018. <https://doi.org/10.1115/1.4039056>.
- [41] Smolarz A, Kotyra A, Wójcik W, Ballester J. Advanced diagnostics of industrial pulverized coal burner using optical methods and artificial intelligence. Exp Therm Fluid Sci 2012;43:82–9. <https://doi.org/10.1016/j.expthermflusci.2012.04.001>.